

Multispectral Thermal Imager Optical Assembly Performance and Integration of the Flight Focal Plane Assembly

Tammy Henson, Les Krumel, and Dick Blake
Sandia National Laboratories, P.O Box 5800, Albuquerque, NM 87185-0980

Don Byrd
Silicon Valley Group, Tinsley Division, 3900 Lakeside Dr., Richmond, CA 94806

Wynn Christensen
Los Alamos National Laboratories, NIS Division, MS C323, Los Alamos, NM 87545

William Rappoport and Gon-Yen Shen
Raytheon Optical Systems, Inc., 100 Wooster Heights Road, Danbury, CT 06810-7589

ABSTRACT

The Optical Assembly (OA) for the Multispectral Thermal Imager (MTI) program has been fabricated, assembled, and successfully tested for its performance, has been integrated into the flight payload structure, and has the flight Focal Plane Assembly (FPA) integrated and aligned to it. This represents a major milestone achieved towards completion of this earth observing E-O imaging sensor that is to be operated in low earth orbit. The OA consists of an off-axis three mirror anastigmatic (TMA) telescope with a 36 cm unobscured clear aperture, a wide-field-of-view (WFOV) of 1.82° along the direction of spacecraft motion and 1.38° across the direction of spacecraft motion, and a comprehensive on-board calibration system. The OA is part of a multispectral pushbroom imaging sensor which employs a single mechanically cooled focal plane with 15 spectral bands covering a wavelength range from 0.45 to 10.7 μm . The OA has near diffraction-limited performance from visible to the long-wave infrared (LWIR) wavelengths. Two key performance criteria, 80% enpixed energy in the visible bands and radiometric stability, drove the design, fabrication, and assembly requirements of the OA. Enpixed energy in the visible bands also drove the alignment requirements of the FPA detectors to the OA image plane to be less than $\pm 20 \mu\text{m}$ over the entire visible detector field of view (FOV). Radiometric stability requirements mandated that a cold Lyot stop be placed in the imaging system for stray light rejection and thermal background reduction. The Lyot stop is part of the FPA assembly and acts as the aperture stop for the imaging system. The alignment of the Lyot stop to the OA drove the centering and to some extent the tilt alignment requirements of the FPA to the OA.

Keywords: Multispectral imaging, remote sensing, space optics

1. INTRODUCTION

This paper describes the MTI system, the performance of the MTI OA, and the integration and alignment of the FPA to the OA. The first section is a general description of the multispectral imaging system. The next several sections describe the OA system and performance, and the integration and alignment of the FPA focal plane and Lyot stop to the OA imaging system. The last section is a summary.

2. MULTISPECTRAL IMAGING SYSTEM GENERAL DESCRIPTION

The three major subsystems that make up the multispectral imaging system are the OA, the FPA, and the cryocooler. The OA provides high quality images from the visible through the thermal IR and also provides a state-of-the-art on-board calibration system (OBCS) to obtain accurate on-board calibration of the entire end-to-end imaging system and also of the FPA alone. The OA was built by Raytheon Optical Systems Incorporated (ROSI).

A cutaway view of the FPA is shown in Figure 1. The FPA consists of a vacuum shroud, a BaF₂ window, a cold shield, a cold stop (Lyot stop), and linear detector arrays with optical filters immediately above the arrays. The detector arrays are

placed at the image plane of the OA. The linear arrays provide spatial resolution in one direction (cross-track). The motion of the pushbroom imaging system relative to the ground produces a scanning operation in the other direction (along-track), thereby producing two-dimensional images in multiple wavelength bands. The BaF₂ window allows the FPA to be evacuated separately and provides additional contamination control for the FPA. The thickness of each individual optical filter is adjusted so that the focal shift due to the nominal dispersion in the BaF₂ window and the optical filter substrates is equalized for all the bands. Thereby the focus is placed at the correct physical location for each detector array material type. The cold shield extends from the detector arrays to the exit pupil of the OA. A cold stop is placed at the exit pupil location. This design reduces the thermal background from the surrounding OA structure by allowing for 100% cold shielding.

TRW.

The linear arrays on the FPA are arranged in three pairs of sensor chip assemblies (SCAs). Each pair of SCAs consists of a visible wavelength to mid-wavelength infrared SCA and a long wavelength infrared SCA. The arrangement of the SCAs on the focal plane is shown in Figure 2. Three pairs of SCAs are used to span the full cross-track field of view. Bands A-D are the visible (VIS) bands whose spectral bandpasses are in the wavelength range of 0.45 - 0.86 μm . Bands E-G are near-infrared (NIR) bands whose spectral bandpasses are in the wavelength range of 0.86 - 1.04 μm . Bands H, I, and O are the short wavelength infrared (SWIR) bands whose spectral bandpasses are in the wavelength range of 1.36 - 2.35 μm . Bands J-K are medium wavelength infrared (MWIR) bands whose spectral bandpasses are in the wavelength range of 3.50 - 5.07 μm . Bands L-N are LWIR bands whose spectral bandpasses are in the wavelength range of 8.00 - 10.7 μm . Silicon photodiodes are used for bands A-D. Indium antimonide is used for bands E-K and O. Mercury cadmium telluride is used for bands L-N. The FPA, which was built by Raytheon Santa Barbara Research Center, is described in further detail in an SPIE paper given by J. Rienstra and M. Ballard¹.

A mechanical cryocooler is used to cool the FPA to a nominal temperature of 75 K. The cryocooler provides over 2.25 watts of cooling power at 65 K. A thermal strap connects the cold block of the cryocooler to a metal pedestal that supports the focal plane. A conservative 10 K increase in temperature across the thermal strap is assumed. The cryocooler also cools the cold shield to reduce the infrared background on the focal plane. The cryocooler uses temperature sensors to provide closed-loop temperature control of the cold block which is designed for low vibration to minimize jitter of the imaging system. The mechanical cryocooler was built by

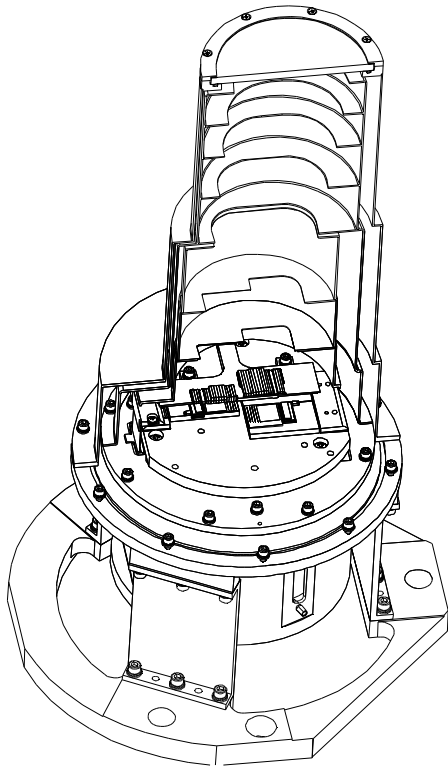


Figure 1. MTI Focal Plane Assembly

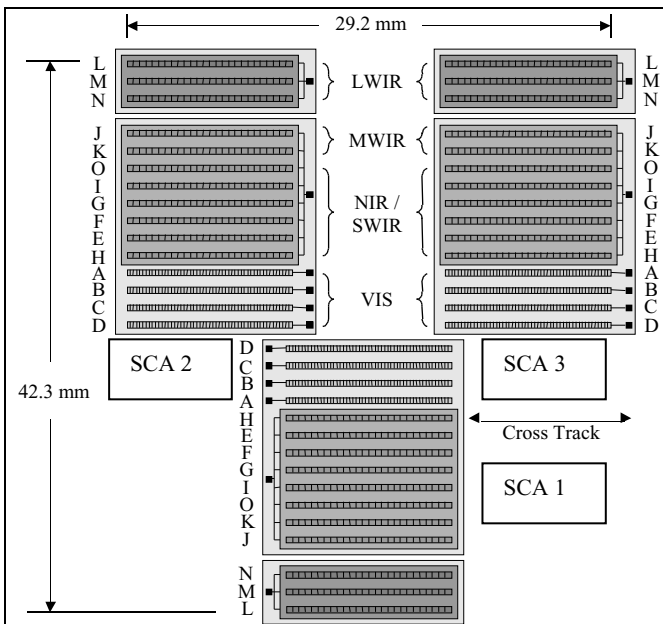


Figure 2. Detector Array layout.

Figure 3 shows the MTI payload in the Class 100 clean area at Sandia National Laboratories (SNL). The OA, FPA, and cryocooler have been fully integrated into the flight payload structure. Payload level assembly and testing has been completed at SNL. The payload has undergone an extensive ground calibration at Los Alamos National Laboratories (LANL) and is now ready for integration to the satellite bus at SNL. Figure 4 illustrates the configuration of the OA system.

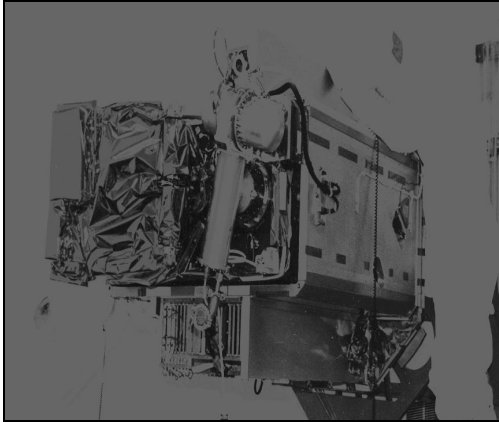


Figure 3. The MTI Payload

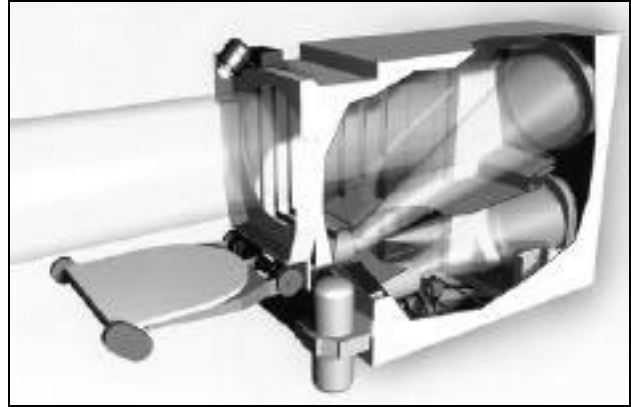


Figure 4. MTI Optical Assembly Configuration.

3. OPTICAL ASSEMBLY SYSTEM DESCRIPTION

The OA consists of an F/3.47 off-axis three mirror anastigmatic (TMA) telescope² with a 36 cm unobscured clear aperture, and a wide-field-of-view (WFOV) of 1.82° along the direction of spacecraft motion and 1.38° across the direction of spacecraft motion. It also has an accessible exit pupil, a flat image plane, and a state-of-the-art on-board calibration system. The primary and tertiary mirrors are eighth-order generalized aspheres, while the secondary mirror is a simple hyperbolic conic section³. The three mirrors share a common optical axis, significantly reducing the complexity during alignment. Both the primary and tertiary mirrors are aggressively lightweighted by 80%. The secondary mirror is mounted to an articulated mechanism capable of $\pm 186\text{-}\mu\text{m}$ focus adjustment at the focal plane.

The main telescope structure is made of graphite cyanate ester composite material. This material provides extremely low thermal expansion and significantly lower dimensional changes due to water compared to graphite epoxy. The structure was fabricated by Alliant Techsystems, Incorporated. The temperature of the structure is actively controlled and continuously monitored with thermal sensors and heaters to maintain a stable background environment within the telescope.

Many of the complex mechanisms of the system stemmed from the need to provide both full aperture, end-to-end and “quick-look” calibrators, covering both visible and infrared wavelengths. The full aperture calibrators are incorporated into the telescope’s unique aperture door subassembly. The door is a double-clamshell design consisting of two motor extended panels, as depicted in Figure 5. The inside of the clamshell is painted white (Z-93P) for solar radiation diffusion. This panel, referred to as the Visible Reflectance Panel (VRP), can be folded or fully extended 180 degrees by a clutch/step motor driver. The top outside of the clamshell is painted black (Chemglaz Z306) to act as a blackbody source. The thermally controlled blackbody source, which is referred to as the aperture blackbody (ABB), is presented to the OA when the door is closed and the VRP is in the folded position. The door can be fully closed or open to 140 degrees during observation by two sets of clutch/motor drivers, one for primary use and one for redundancy.

For infrared band calibration, the blackbody is presented to the OA. The surface of the blackbody is precisely temperature controlled with heaters and thermistors to the pre-designated calibration temperature. During the visible calibration, the door is partially opened to 45 degrees and the VRP unfolded, exposing a white, diffused surface to receive the solar radiation at approximately a 47.5-degree compounded angle. The white surface diffusion characteristics are periodically calibrated with the Visible Reflectance Panel Monitor (VRPM) mounted on the door frame, which compares the irradiance of the solar illuminated panel to direct irradiance from the sun in five spectral bands ranging from $0.45\ \mu\text{m}$ to $0.96\ \mu\text{m}$ wavelength.

During launch, the door is secured by a locking mechanism and will be released after the spacecraft reaches its operating orbit. During operations in space, the door is nominally closed to minimize heat leaks, and opened only during observation. In case of motor failure, the clutch can be de-energized and the door will spring open, as an extra safety measure. Similarly, the VRP goes to a closed position in the fail-safe mode.

The quick-look calibrators are used for immediate reference before and after scene imaging at both visible and infrared bands. The design has a five-position calibration wheel subassembly (Figure 6) located in front of the cold stop window of the focal plane dewar. The first position on the wheel, the fail-safe position, is an open position for viewing the far field. In the next position, a retro-reflection mirror is used to reflect the cryogenically cooled dewar back into the focal plane thereby providing a near zero reference for the focal plane detectors. Thermistors on this mirror allow corrections for the mirror's thermal contribution to the narcissistic scene. The next two positions contain identical blackbody sources for thermal infrared calibration. These sources include a germanium lens that images the blackbody onto the focal plane. The blackbodies are temperature controlled and commandable up to 380 degrees Kelvin. Nominally, the two blackbodies are maintained at different temperatures which bracket the expected scene temperature. The last wheel position is for VNIR and SWIR calibration. It contains a lens and fold mirror which image the exit port of an integrating sphere assembly located off the wheel onto the focal plane. Both primary and secondary stabilized lamps are located in the integrating sphere to provide a uniform stable VNIR/SWIR illumination source. Photodiodes, which sense the lamp's intensity, are used in a feedback loop to provide a stable radiometric output and color temperature correction.

The calibration wheel is a highly reliable mechanism driven by a set of clutch/step motor drivers (same design as the door subassembly, one primary and one for redundancy). The positioning of the various sources has been calibrated and shown to be very repeatable to minimize errors at the focal plane. Again, the wheel has a clutch and a fail-safe spring that returns the wheel to its open position in case of motor failure.

4. OPTICAL ASSEMBLY PERFORMANCE

The OA underwent extensive testing to ensure that its two most critical performance requirements, image quality and calibration source stability, were met. The wavefront of the OA was measured over the FOV after assembly and again after the temperature cycling and random vibration/shock tests were complete. The wavefront tests demonstrated that the MTI OA met the imaging quality requirement of 80% enpxeled energy in the visible bands (12.5- μ m pixels) and 84% enpxeled energy in the infrared bands (50- μ m pixels, 84% in 100 μ m square in the LWIR).

Utilizing the as-built OA prescription, the wavefront data taken across the FOV, and the as-built FPA parameters, the MTF was determined at the Nyquist frequency for all 15 spectral bands at several field locations and then compared with the diffraction MTF at those field locations. The Nyquist frequency is determined by the size of the pixel used to sample the image. For the visible bands A - D the Nyquist frequency is 40 cycles/mm, and for the infrared bands E - O the Nyquist frequency is 10 cycles/mm. Figure 7 shows the average MTF at Nyquist frequency of the as-built OA/FPA across the FOV for each spectral band of the system. The average diffraction-limited MTF at Nyquist frequency across the FOV for each

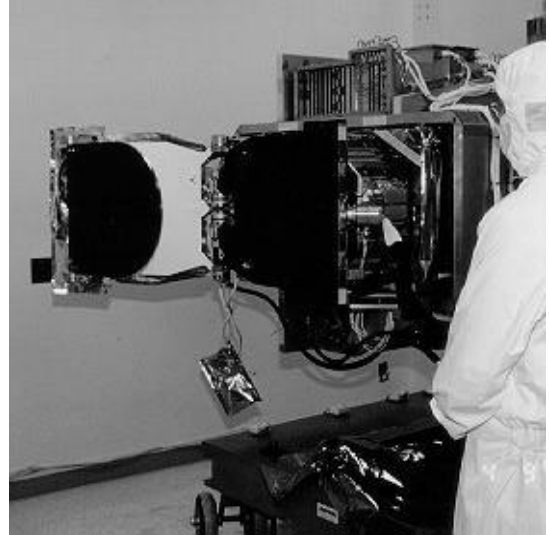


Figure 5. Baffle and Double-Clamshell Aperture Door



Figure 6. The quick-look calibration wheel subassembly provides immediate calibration before and after imaging.

spectral band is also shown for comparison. It is clear to see that the performance of the as-built OA/FPA is diffraction-limited beyond about 0.9 μm wavelength at the Nyquist frequency.

The calibration hardware underwent extensive testing to assure it would meet the radiometric stability requirements. All radiometric stability requirements are relative to the LANL ground calibration that was performed with NIST traceable sources.

The stability of the quick calibration visible source was tested across its full field before and after subassembly vibration and also before and after wheel repositioning. The irradiance values repeated within the budgeted $\pm 0.7\%$ across the required 42-mm field.

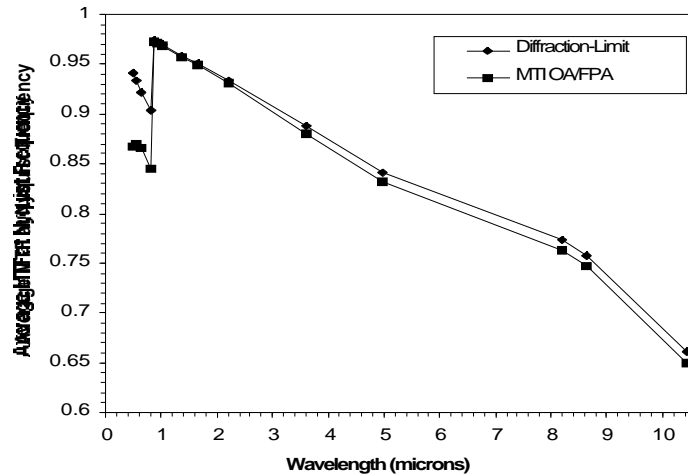


Figure 7. Average MTF at Nyquist frequency compared to the diffraction-limit across the FOV for each spectral band.

The bi-directional reflectance distribution function (BRDF) of the VRP was characterized at ROSI. SNL measured the field of view and spectral response of the VRPM. Together ROSI and SNL verified the VRP/VRPM solar spectral responsivity by calibrated source measurements at ROSI and solar measurements at SNL.

The quick calibration blackbodies were qualified as a subassembly for radiometric stability and uniformity. Short term stability of the measurement detector in combination with the quick calibration blackbodies showed a max variation of 0.04% over a two hour period with an RMS measurement precision of approximately 0.006%. Uniformity of the quick calibration blackbodies were approximately 0.17%/mm and 0.2%/mm for the along track and cross track directions, respectively. The specified irradiance uniformity in the focal plane was 0.2%/mm.

The IR calibration source performance depends on stable thermistors. SNL confirmed the stability of the thermistors to 50 mK in their mounted configuration under temperature cycling ($-50\text{ }^{\circ}\text{C}$ to $+110\text{ }^{\circ}\text{C}$) and vibration by measuring the resistance of the thermistors in a well controlled ice bath at every stage of fabrication and testing. Continued monitoring of the ABB and quick calibration blackbody temperatures while the OA was undergoing ground calibration at LANL for several months has shown that the sources are extremely stable. Their measured stability has been within the 50 mK thermistor stability measured at SNL.

Detailed descriptions of the optical design, fabrication, assembly, and testing are described in an earlier paper⁴ presented at the SPIE San Diego Conference in 1998.

5. FOCAL PLANE ASSEMBLY TO OPTICAL ASSEMBLY ALIGNMENT

5.1 FPA focal plane to OA image plane alignment

Alignment of the FPA to the OA in a rudimentary sense involves placement of a focal plane at the image plane of a telescope. The allowable tolerance zone was 20 μm over the entire visible detector FOV with a goal of less than 10 μm over the entire Band D FOV. The “focal plane” is comprised of a myriad of detector elements or arrays. The focal plane is expeditiously placed at the “image plane” of the telescope to record the image. The subject of the FPA/OA alignment therefore involves coordination of two respective planes, centration, and a “clocking” rotation around the optical axis. The alignment setup is shown in Figure 8. Sophisticated equipment such as a collimated light source, steering mirror whose angular displacement was monitored by Differential Measuring Interferometers (DMI) to an accuracy of 0.06 arc-seconds, feedback from the detector elements, and an electro-mechanical manipulator for FPA placement were utilized during the alignment process. The alignment was all performed remotely outside of the class 100 clean area.

The first objective is to bring the focal plane of the FPA into coincidence with the image plane of the OA. Physical alignment with external features provides an initial orientation. Intrinsic to the OA, collimated light is focused to converge onto a point in space, with divergence occurring behind it. The focal point is shaped like the waist of an hourglass. If one of

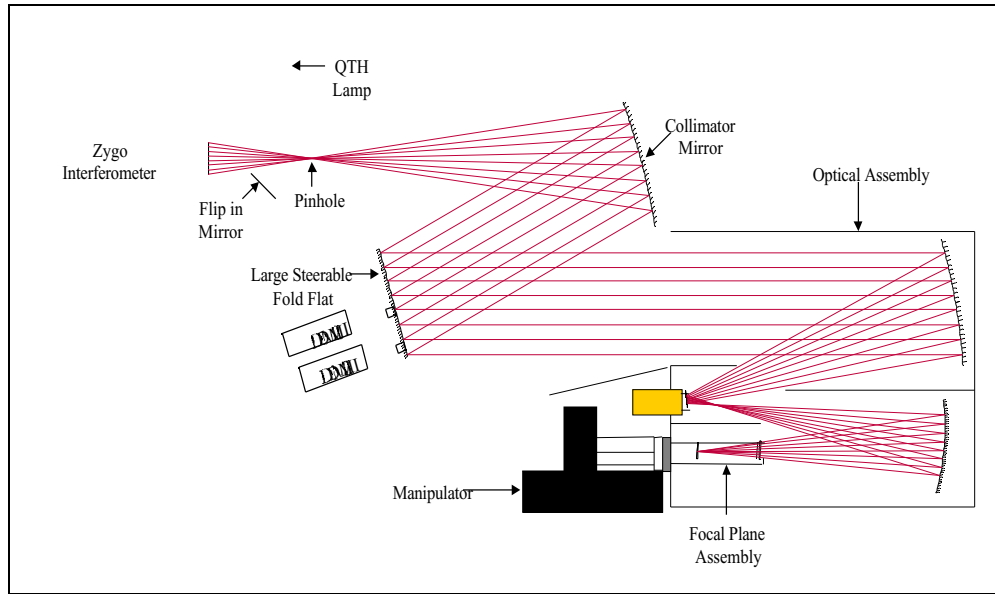


Figure 8. MTI OA/FPA Alignment Setup.

the detector pixels moves along the beam, an assumption is made that the signal intensity is a measure of focus; where the most energy is collected is also the apex of convergence. By directing the input to three arbitrary field angles, three corresponding focal points are determined. By definition, these three points can be used to represent the image plane. Moving the FPA detectors along the chief ray of the OA provides quantitative measurements of where the image plane lies. Orientation of the FPA is accomplished with the manipulator, a precision robotic device.

The manipulator moves the FPA along the optical axis with an accuracy of about 100 nm. Each of three selected focal points of the OA is measured in succession with a known field angle and corresponding detector pixel of the FPA. Displacements of the three detector pixels to these focal points are independent of one another. Comparison between these measurements serves as an indication for out-of-plane alignment error. Ideally, if all three differences were similar, the planes would be parallel with only some common separation. With vector analysis an equation is formed for the plane of the FPA using the three differences and known topology of the detector arrays. Projection of this onto the existing coordinate frame of the manipulator provides values for two rotations necessary to mitigate the error. The manipulator is designed with six degrees of freedom (DOF). Rotations occur on a pivot point removed from the FPA/OA interface due to physical limitations. An orthographic arrangement of linear actuators with 100 nm accuracies and 200 mm lever arms provide capability of 0.5 mrad angular resolution in three axes. Yet, because of the lever arm, any angular correction necessitates some amount of translation, which is easily calculated.

Light was directed near the center of SCA 1 and near the outer edges of SCA 2 and SCA 3 in order to provide the most sensitive measurement of tilt errors. Measurements in focus were made by systematically stepping the focal plane along the z-axis over a range of about 200 μm with the manipulator. One complication to the process was added since the optical axis is not truly perpendicular to the image plane. Therefore, the detector pixel was centered on the focused spot by judiciously employing a lateral search routine with the manipulator for every step in the z direction in order to find the local maximum intensity. This procedure was repeated using a white light source for the VNIR/SWIR bands and a blackbody source for checking the MWIR/SWIR bands. These measurements were plotted, illustrating an optimum value for corrections in tip or tilt.

Band A was primarily used for the focus measurements because it has the smallest depth of focus and is therefore the most sensitive band to changes. It is also the band that is the farthest out on the focal plane in the along-track direction of all the visible bands. The LWIR bands, although they are located on the edge of the focal plane, were less sensitive to tilt measurements than Band A due to their larger pixel size and depth of focus. Band D was utilized for the final z position once the tilt was removed. This is because Band D is the band with the least amount of margin for enpixed energy. We were able to get all the visible detectors aligned to about $\pm 10 \mu\text{m}$ over the entire visible FOV. However, due to a problem with

centering the Lyot Stop, which will be discussed further in the next section, an additional along-track tilt error between the image plane of the OA and the focal plane of the FPA had to be added. With the additional tilt the final alignment error over the entire visible detector FOV is approximately $\pm 20 \mu\text{m}$, with the alignment error over the Band D FOV being approximately $\pm 12 \mu\text{m}$.

With the FPA and image plane aligned, initial centering of the FPA was a straightforward process, irrespective of the fact that no detector elements existed at the center of the FPA. Once the Line of Sight (LOS) was established, mapping of field angles to the image plane was performed to determine desired position of various FPA detector elements. Measurements were made (through readouts on the manipulator) between actual and expected locations for known field angles. Lateral corrections were made with the manipulator in both coordinate axes. However, centering of the Lyot stop is more critical than the centering of the detector arrays. Final centering of the focal plane was accomplished by properly centering the Lyot stop as is described in the next section.

Clocking between the FPA and OA is a matter of rotating the FPA around the z-axis, so that the x and y axes of the FPA focal plane are coincident with the x and y axes of the OA image plane respectively. The steering mirror was successively directed for focus on opposite ends of the focal plane (y-axis). Detector elements at those locations were moved by the manipulator x-axis to measure any lateral offset. Any difference between these measurements at opposite ends of the array exhibit a clocking error. The angle is determined with trigonometry, along with a translation of half the difference in offset. Using the methods described here, the geometric solution converged in each case after just two iterations: one coarse, and another fine.

Once the alignment was complete, the assembly was fixed laterally by setting epoxy dowells, and the manipulator was removed. Polished shims were made to within $.000050''$ and the FPA was bolted onto the OA with the flight shims installed. Alignment verification was accomplished at this point utilizing the secondary mirror assembly (SMA) focus adjustment mechanism and using the large steering mirror to centroid the light on a predetermined focal plane pixel. The SMA moves the secondary mirror in and out of the telescope along the optical axis in steps of $0.75 \mu\text{m}$. This moves the focus at the image plane by $2 \mu\text{m}$ per step. The focus at three points was measured moving the SMA in steps of 10 or moving the image plane in $20 \mu\text{m}$ steps again over a range of about $200 \mu\text{m}$.

A pixel peaking algorithm was developed to accurately centroid the light on a given pixel. Peaking is the methodology for locating the pixel center. Peaking is accomplished by positioning a spot of light on the pixel at the location where the pixel response to the light is maximized. In general terms, the peaking exercise was accomplished by positioning a $20 \mu\text{m}$ spot of light in the vicinity of the pixel, performing a raster-scanned pattern across the pixel and calculating the spatial centroid of the samples. The centroid should be very close to the position of greatest response for the pixel and should also be very close to the pixel center. The goal of the peaking effort was to find the centroid to within 20% of the pixel diameter. For the $12.5 \mu\text{m}$ diameter pixels this would mean within $2.5 \mu\text{m}$.

The equipment setup for this measurement is shown in Figure 9. The setup can be broken down into three areas, the fold mirror positioning system, the fold mirror position measurement system, and the controller. The fold mirror uses piezo-electric drive technology and has fine motor resolution equivalent to approximately 0.005 arc-sec of fold mirror rotation. The position of the mirror is measured with a Distance Measurement Interferometer (DMI) configured to measure angles. The DMI has a resolution of 0.06 arc-sec.

The measurement environment was fairly noisy mainly due to mechanical vibrations. Any disturbance that caused the spot of light to move created problems for the measurement. Mechanical vibrations on the mirror mounts and supporting structures would cause noise in both the pixel output and the mirror position measurement. In order to reduce the effect of the noise, the mirror position obtained from the DMI used a 40-sample average and the pixel signal was the result of 16 averaged samples. Repeatability of less than 0.1 arc-sec was obtained in this environment.

We experimented with several algorithms for finding the pixel centers. The algorithm that we chose to use, the raster scan method, has the drawback that it is slower than the other algorithms but it is also more accurate in a noisy environment and is more verifiable. As the raster scan is being executed, the operator is able to see the strength of the signal at each measurement position and visually verify the result to gauge the quality of the data (see Figure 10). The algorithm incorporates some compromises. Small sample spacing in the raster-scan results in higher measurement resolution but takes longer to finish. During the actual measurements, we varied the sample spacing so we could do a quick 'roughing in' of the

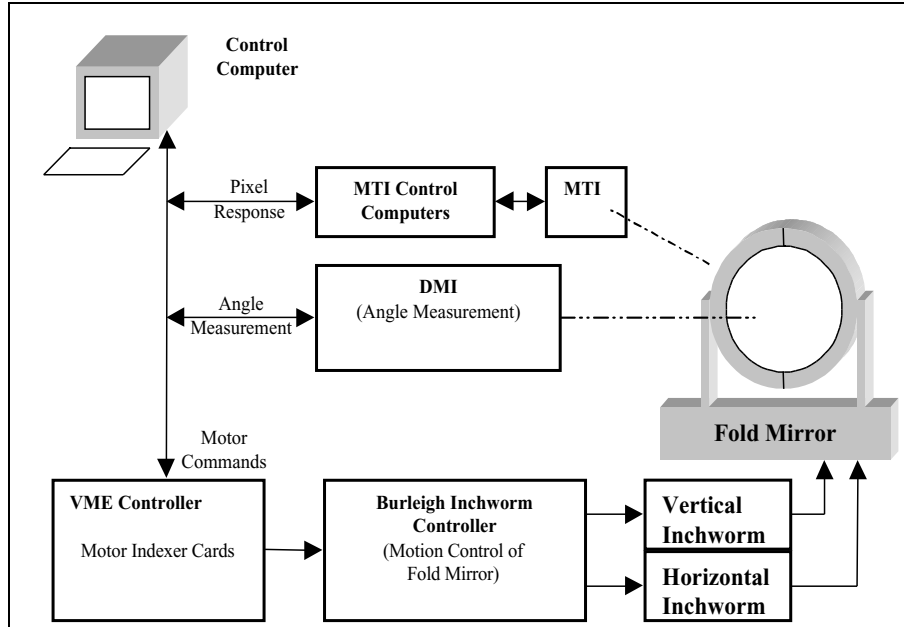


Figure 9. Peaking Equipment Setup

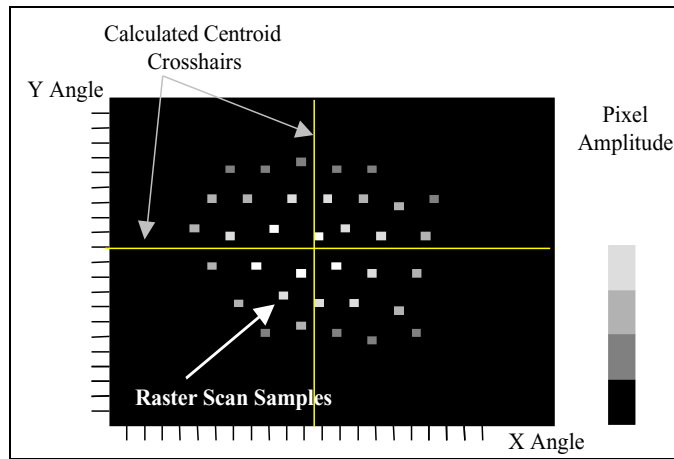


Figure 10. Peaking computer display showing samples and resultant centroid

pixel, in case the pixel wasn't totally inside the raster scanned area. Then we re-centered the scan and reduced the sample spacing to get more accurate results. The raster-scan algorithm is less susceptible to noise than the other algorithms because it does not require a series of decisions based on amplitude. The centroid position calculation is based on the results of every sample and therefore the noise in the samples is reduced through averaging. The equation for calculating the centroid position is as follows:

$$X_{centroid} = \frac{\sum_{j=1}^n \sum_{k=1}^m I_{jk} X_{pos_{jk}}}{\sum_{j=1}^n \sum_{k=1}^m I_{jk}} \quad (1)$$

where I equals the pixel intensity and X_{pos} equals the pointing mirror angular position.

Utilizing this process, the focus position was verified after the FPA was installed with flight shims. The MTI payload was then taken into thermal vacuum and the focus measurements were repeated. We discovered that we had a larger than expected focus shift between the laboratory environment and operation in vacuum at operating temperature. The best focus position was at the end of travel for the SMA focus adjustment mechanism. Therefore, we had to re-shim the focal plane in order to place the best focus position back at the center of travel of the SMA. We still do not completely understand why we had such a large focus shift between laboratory and operating environment. We suspect it may be due to larger dimensional change in the graphite cyanate ester composite structure with moisture outgassing than was expected. After the final shimming, we were able to maintain the alignment of the Band D detectors in all 3 SCA's to the image plane to $\pm 12 \mu\text{m}$.

5.2 FPA Lyot stop alignment

The Lyot stop of the FPA acts as the aperture stop for the imaging system. It is part of the FPA assembly. The stop is located approximately 200 mm in front of the focal plane. There are no independent adjustments between the stop and the focal plane assembly. So tilts in the focal plane can cause large lateral displacements of the stop due to the long lever arm. Centering of the Lyot stop is even more critical than the centering of the focal plane. This is because the image of the Lyot stop formed by the OA in object space (which is the entrance pupil) needs to be within the primary mirror for all field positions. Otherwise some field positions would be able to see the warm telescope structure. This would be detrimental to our thermal calibration accuracy requirements.

Therefore, we devised a method whereby we could map out the location of the entrance pupil on the primary mirror for various field positions and move the FPA laterally in order to properly center the Lyot stop. We did this by viewing the entrance pupil position on the primary mirror with a theodolite. We very accurately aligned the theodolite along a particular field of view at the extreme edges of the focal plane. We would then translate the theodolite so that one extreme edge of the entrance pupil was located on the cross hair. We would then record the position of the theodolite. Then we would translate the theodolite so that the edge of the primary mirror was located on the cross hair. Recording the difference in the theodolite position between the entrance pupil measurement and the primary mirror measurement told us the relative position of the edge of the entrance pupil on the primary mirror. We repeated this measurement for the extreme horizontal and vertical positions of the entrance pupil at four different field points. The fields used were the corners of SCA 1 and the outer corners of SCA's 2 and 3 for Band L, the band furthest out on the focal plane.

When we completed the initial alignment of the FPA focal plane to the OA image plane, we then mapped out the position of the entrance pupil on the primary mirror. We found that for some field positions the entrance pupil was off of the primary mirror. We moved the FPA laterally to try to correct for the misalignment, but found that we would have to move the FPA more than the bolt holes between the FPA and the OA would allow. We believe the problem may have been caused by a larger than expected tilt between the as-built image plane and the OA mounting interface. Since the Lyot stop is not independently adjustable from the focal plane, we found that we would have to purposely add some slight along-track tilt misalignment between the focal plane and the image plane in order to translate the Lyot stop enough so that the entrance pupil stayed on the primary mirror with the bolt holes lined up. We calculated how much translation would be needed and adjusted the angle of the FPA accordingly. We then re-verified the focus error across the focal plane SCA's, and found that we had added an additional $\pm 10 \mu\text{m}$ of focus error to the alignment between the focal plane and the image plane across the field of view. However, we were able to align the Lyot stop to within $150 \mu\text{m}$ of the best possible location and ensure that the entrance pupil remained on the primary mirror for all field positions. Once the Lyot stop alignment was complete, the assembly was fixed laterally by setting epoxy dowels.

The Lyot stop alignment was checked again after the FPA was bolted onto the OA with the flight shims and after the focal plane was re-shimmed. The Lyot Stop remained properly centered and no additional tilt between the FPA and the OA was produced.

SUMMARY

In summary, the MTI OA has been fabricated, assembled, and successfully tested for its performance, has been integrated into the flight payload structure, and has the MTI flight FPA integrated and aligned to it. All performance parameters meet or exceed the specifications. The image quality is near diffraction limited in the visible at the Nyquist frequency and is

strictly diffraction limited above 0.9 μm wavelength at the Nyquist frequency. The on-board calibration sources have demonstrated very good stability and uniformity. The focal plane of the FPA has been aligned to the image plane of the OA to within $\pm 20 \mu\text{m}$ over the entire visible detector FOV and to within $\pm 12 \mu\text{m}$ over the critical Band D FOV. The Lyot stop has been centered in the system to within $\pm 150 \mu\text{m}$ and the entrance pupil is located on the primary mirror at all times so that the FPA can never see the warm telescope structure which is critical for accurate thermal calibration. The MTI payload is fully assembly, has undergone extensive ground calibration at LANL, and is currently being prepared for integration with the spacecraft bus.

REFERENCES

1. J. Rienstra and M. Ballard, "MTI Focal Plane Assembly Design and Performance", SPIE Proc. Vol. 3753, 1999.
2. K. Shu, and T. Henson, "Optical design for a Visible through Thermal Infrared Multi-Band Imaging System", SPIE Proc. Vol. 2863, pp. 301-310, 1996.
3. J. Magner, and T. Henson, "Optical fabrication and metrology for a Visible through Thermal Infrared Multi-Band Imaging System", SPIE Proc. Vol. 3377, pp. 258-266, 1998.
4. T. Henson, S. Bender, D. Byrd, W. Rappoport, G. Shen, "Optical Assembly of a Visible through Thermal Infrared multispectral Imaging System", SPIE Proc. Vol. 3439, pp. 70-78, 1998.

Sandia is a multiprogram laboratory operated by Sandia Corporation, a Lockheed Martin Company, for the United States Department of Energy under Contract DE-AC04-94-AL85000.